Giant Enhancement of the Goos-Hänchen Shift Assisted by Quasibound States in the Continuum

Feng Wu,[1] Jiaju Wu,[1] Zhiwei Guo,[1] Haitao Jiang,[1,*] Yong Sun,[1] Yunhui Li,[1] Jie Ren,[2] and
Hong Chen[1,†]

[1]*MOE Key Laboratory of Advanced Micro-Structured Materials, School of Physics Science and Engineering,
Tongji University, Shanghai 200092, China*
[2]*Center for Phononics and Thermal Energy Science, China-EU Joint Center for Nanophononics, Shanghai Key
Laboratory of Special Artificial Microstructure Materials and Technology, School of Physics Science and
Engineering, Tongji University, Shanghai 200092, China*

We achieve reflection-type bound states in the continuum (BICs) in the compound grating waveguide structure by tuning the excitation of the guided modes. Assisted by the quasi-BICs with ultrahigh Q factors, the Goos-Hänchen (GH) shift can be greatly enhanced to larger than or equal to four orders of wavelength. In addition, different from the large GH shift based on the Brewster dip or transmission-type resonance, the maximum GH shift assisted by the reflection-type quasi-BIC is located at the reflectance peak with unity reflectance, which can be more easily detected in the experiment. Based on the quasi-BIC-assisted giant GH shift, we propose an ultrasensitive temperature sensor with a minimum resolution in the order of 10^{-4} °C. Our work provides a route, under the current experimental conditions, to design ultrasensitive sensors, light information storage devices, wavelength division de/multiplexers, optical switches, and polarization beam splitters based on this giant GH shift together with high reflectance.

I. INTRODUCTION

When a light beam is totally reflected by a dielectric, it will undergo a lateral shift from the position predicted by geometrical optics in the incident plane. This shift is known as the Goos-Hänchen (GH) shift and was first observed experimentally in 1947 [1]. The GH shift has attracted tremendous attention due to the potential applications in a variety of sensors [2–4], optical information storage [5], wavelength division de/multiplexer [6], optical switch [7,8], and polarization beam splitter [9]. According to the stationary phase method, the GH shift is proportional to the partial derivative of the reflection phase to the incident angle [10]. In the case of total internal reflection, the GH shift is usually comparable to the wavelength [1]. This tiny GH shift poses a challenge in the experimental measurement. Therefore, the enhancement of the GH shift is highly desirable. Up until now, there are two main mechanisms to greatly enhance the GH shift. One is based on the Brewster angle effect. The GH shift can be enhanced to larger than or equal to one order of wavelength near the Brewster angle [11–14]. The other is based on transmission-type resonance with a transmission peak. Previous research has shown that the reflection

phase will dramatically vary around the incident angle of the resonance peak [15]. As a result, a high-Q-factor resonance will lead to a large GH shift in a transmission-type resonance structure. According to this physical mechanism, various microstructures have been proposed to greatly enhance the GH shift, including a weakly absorbing slab [16], one-dimensional photonic crystal with defect [17], surface plasmon resonator [18,19], asymmetric double prism [20], photonic crystal slab [21], metal cladding waveguide [2], Bloch surface wave resonator [22], epsilon-near-zero metamaterial slab [23], and dielectric slab (for Laguerre-Gaussian beams) [24,25]. However, in these two mechanisms, there is a common shortcoming in that the maximum GH shift is exactly located at the transmittance peak (i.e., reflectance dip). The reflectance in some of the above works is even less than 0.1%, which is too weak for detecting the reflected beam experimentally although the GH shift can be enhanced to larger than or equal to two orders of wavelength [12,13,16,17]. Can we overcome this shortcoming to greatly enhance the GH shift while maintaining high reflectance at the same time based on another mechanism?

In recent years, localized resonance modes inside the continuous spectra that are called bound states in the continuum (BICs) have attracted researchers' interest [26]. In 1985, Friedrich and Wintgen realized BICs by using a generic two-level non-Hermitian Hamiltonian

*jiang-haitao@tongji.edu.cn
†hongchen@tongji.edu.cn

[27,28]. Their approach was applied to a photonic waveguide system by Bulgakov *et al.* [29] in 2008 and was experimentally demonstrated by Plotnik *et al.* in 2011 [30]. In 2008, Marinica *et al.* also theoretically proposed a Fabry-Perot mechanism for BICs in a double array of dielectric rods [31]. Although true optical BICs with a vanishing resonance width (i.e., infinite Q factor) are mathematical objects, quasi-BICs with ultranarrow resonance widths can be utilized in many applications, including surface-emitting lasers [32,33], filters [34], absorbers [35], nonlinear optical devices [36], and various sensors [37–39]. For example, Romano *et al.* achieved sensitive refractive index sensing in the all-dielectric metasurface that supports BIC [38]. In addition to a transmission-type resonance, BIC can be a reflection-type resonance with a reflection peak. A variety of structures have been proposed to achieve reflection-type BICs, such as a two-part periodic grating [40–43], asymmetric grating [44–46], photonic crystal slab [32,42,47–51], and metasurfaces [37,52]. In 2016, Ni *et al.* investigated the formation of BICs at off-Γ points in two-part periodic gratings and photonic crystal slabs by using a semianalytical coupled-wave theory framework [42]. Later, Wang *et al.* realized quasi-BICs in an asymmetric slotted high-contrast grating and found that the corresponding Q factor can be flexibly tuned by the degree of asymmetry [45]. Very recently, Koshelev *et al.* revealed that metasurfaces composed of seemingly different meta-atoms with broken in-plane inversion symmetry can possess quasi-BICs [52]. In this paper, we achieve reflection-type quasi-BICs in a compound structure composed of a four-part periodic grating layer and a waveguide layer without breaking the in-plane inversion symmetry. When the four-part periodic grating reduces to a two-part periodic grating by changing the geometric parameter, the grating-induced basic vector of the reciprocal lattice will double. As a result, the previously excitable odd-order guided resonance modes cannot be excited. These discrete dark modes are BICs with an infinite Q factor. Very near BICs, the resonance modes have ultranarrow resonance widths (i.e., ultrahigh Q factors) and they are called quasi-BICs. Subsequently, we demonstrate that the GH shift can be greatly enhanced to larger than or equal to four orders of wavelength assisted by the quasi-BICs because the reflection phase dramatically changes around the incident angle of the resonance peak. Different from the large GH shift fulfilled by the Brewster dip [11–14] or transmission-type resonance [15–23], the maximum GH shift realized by the reflection-type quasi-BIC is located at the reflectance peak with unity reflectance, which can be more easily detected in the experiment. As an example of application, we design an ultrasensitive temperature sensor based on the quasi-BIC assisted giant GH shift.

This paper is organized as follows. In Sec. II, we discuss the physical mechanism of the BICs in the compound grating waveguide structure in detail. In Sec. III, we utilize the ultrahigh Q factors of quasi-BICs to achieve a giant enhancement of the GH shift. In Sec. IV, on the basis of the quasi-BIC-assisted giant GH shift, we design an ultrasensitive temperature sensor with minimum resolution in the order of 10^{-4} °C. Finally, the conclusion is given in Sec. V.

II. BIC IN COMPOUND GRATING WAVEGUIDE STRUCTURE

The unit cell of the compound structure composed of a grating layer and a waveguide layer is shown in Fig. 1. The first layer is a four-part periodic grating layer with the grating period $\Lambda = 400$ nm and the thickness $h_1 = 290$ nm. The first and third parts are high-index HfO$_2$ with the refractive index $n_H = 1.975$ [53], while the second and fourth parts are air. We choose HfO$_2$ for the grating material because it can be fabricated with high quality by the focused ion beam milling technique [54]. The widths of the first and third parts are the same value d_a, while those of the second and fourth parts are $d_b = d + \Delta d$ and $d_c = d - \Delta d$, respectively. Here, we set $d_a = 0.2\Lambda$ and obtain $d = 0.3\Lambda$. We define the tunable geometric parameter $\delta = \Delta d/d \in [-1, 1]$ to reflect the difference between the second and fourth parts of the grating unit cell. The second layer is a HfO$_2$ waveguide layer with the refractive index $n_{WG} = 1.975$ and the thickness $h_2 = 160$ nm. The substrate medium is SiO$_2$ with the refractive index $n_S = 1.46$. It should be pointed out that the proposed structure does not break the in-plane inversion symmetry because the width of the first part of the grating layer is the same as the third one. The incident plane is the x-O-z plane. Without loss of generality, we only consider that a TE-polarized (electric field parallel to the y direction) light obliquely launches onto the structure at an incident angle θ.
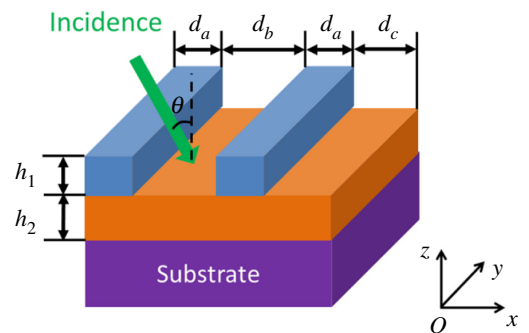

FIG. 1. Schematic of the unit cell of the compound grating waveguide structure. The first layer is a four-part periodic grating layer with the grating period Λ and the thickness h_1. The widths of the first and third parts are the same value d_a, while those of the second and fourth parts are $d_b = d + \Delta d$ and $d_c = d - \Delta d$, respectively. The second layer is a waveguide layer with the thickness h_2.
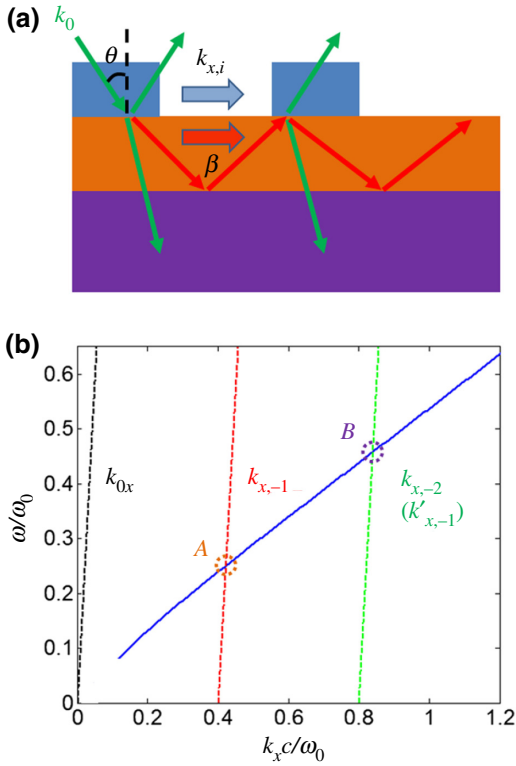
FIG. 2. (a) GMR excitation of the compound grating waveguide structure. $k_{x,i}$ and β represent the tangential components of the wave vectors in the grating and the waveguide layer, respectively. (b) Dispersion relations of the TE_0 guided mode in the waveguide layer (blue solid line), $k_x = k_{0x}$ in the air background (black dashed line), and $k_x = k_{x,i}$ ($i = -1, -2$) in the grating (red and green dashed lines).

Figure 2(a) gives the schematic of the guided mode resonance (GMR) excitation of the compound grating waveguide structure. The tangential component of the wave vector in the system is denoted by k_x. In the air background, $k_x = k_{0x} = k_0 \sin\theta$, where $k_0 = \omega/c$ is the wave vector in air. ω is the angular frequency and c is the speed of light in air. In the grating, $k_x = k_{x,i} = k_{0x} - i \cdot 2\pi/\Lambda$ ($i = \pm 1, \pm 2, \ldots$), where $2\pi/\Lambda$ denotes the basic vector of the reciprocal lattice induced by the grating. In the waveguide layer, $k_x = \beta$, where β represents the propagating constant of the guided mode. With the extra tangential wave vector induced by the grating, the incident light can have resonance coupling to the guided modes. The tangential wave vector (phase) matching condition of the GMR for $\delta \neq 0$ can be expressed as [55]

$$k_{x,i} = k_0 \sin\theta - i\frac{2\pi}{\Lambda} = \beta \quad (i = \pm 1, \pm 2, \ldots). \quad (1)$$

The incident angle is chosen to be $\theta = 5°$. Without loss of generality, here, we only consider the TE_0 guided mode for $\beta > 0$. The dispersion relation of the TE_0 guided mode in

the waveguide layer can be determined by [56]

$$h_2\sqrt{k_0^2 n_{WG}^2 - \beta^2} = \text{atan}\left(\frac{\sqrt{\beta^2 - k_0^2 n_0^2}}{\sqrt{k_0^2 n_{WG}^2 - \beta^2}}\right)$$
$$+ \text{atan}\left(\frac{\sqrt{\beta^2 - k_0^2 n_S^2}}{\sqrt{k_0^2 n_{WG}^2 - \beta^2}}\right), \quad (2)$$

as shown by the blue solid line in Fig. 2(b). Here, we set $\omega_0 = 2\pi c/h_2$. The dispersion relation is cut off at $\omega_{cut} = 0.081\omega_0$. The dispersion relations for $k_x = k_{0x}$ in the air background and for $k_x = k_{x,i}$ ($i = -1, -2$) in the grating are shown by dashed lines in Fig. 2(b). The crossing point between the dispersion relations $k_{x,i}$ and β represents the satisfaction of the GMR condition, which is called the ith order guided resonance mode. Here, we just give the guided resonance modes of the first two negative orders marked by A and B in Fig. 2(b). The corresponding angular frequencies are $\omega_A = 0.250\omega_0$ ($\lambda_A = 640$ nm) and $\omega_B = 0.458\omega_0$ ($\lambda_B = 349$ nm), respectively.

For the proposed structure, the period of the four-part periodic grating layer remains Λ when the parameter $\delta \neq 0$. However, in the case of $\delta = 0$, the four-part periodic grating reduces to the two-part periodic grating with a new period $\Lambda' = \Lambda/2$. The GMR condition is changed to

$$k'_{x,i} = k_0 \sin\theta - i'\frac{4\pi}{\Lambda} = \beta \quad (i' = \pm 1, \pm 2, \ldots). \quad (3)$$

It can be seen that the grating-induced basic vector of the reciprocal lattice doubles when the period of the grating changes from Λ to $\Lambda/2$. The new dispersion relation $k'_{x,m}$ completely overlaps the previous even-order dispersion relation $k_{x,2m}$ ($m = \pm 1, \pm 2, \ldots$). This means that $k_{x,-2}$ becomes k'_{-1} and the GMR condition can still be satisfied at crossing point B. However, the GMR condition cannot be satisfied at point A. As a result, when the geometric parameter δ changes from a nonzero value to zero, the negative first-order guided resonance mode A and other high odd-order modes cannot be excited and become dark modes, whereas the negative second-order guided resonance mode B and other high even-order modes can still be excited. Next, we will study the variance of the Q factor of the resonance when the four-part periodic grating reduces to a two-part periodic grating.

Now, based on the rigorous coupled wave analysis (RCWA) [57], we calculate the reflectance spectra (zero-order diffraction) around λ_A of the structure as the geometric parameter δ changes from 1 to 0 at $\theta = 5°$ for TE polarization, as given in Fig. 3. In addition, the intensity distributions of the electric field in the y direction ($|E_y|$) corresponding to the reflectance peaks are calculated by RCWA are shown in the right insets. The structure is

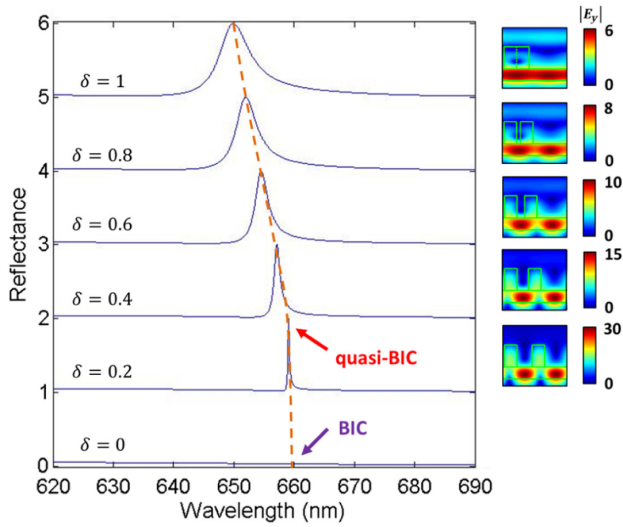FIG. 3. Reflectance spectra (zero-order diffraction) around λ_A of the structure for different values of δ at $\theta = 5°$ for TE polarization. The right insets represent the $|E_y|$ distributions corresponding to the reflectance peaks.

depicted by green lines. The incident electric field intensity is set to be $|E_y^{\text{inc}}| = 1$. It is seen that the reflectance spectra exhibit asymmetric Fano line shapes, which originate from the interference between two channels [58]. One is a narrowband channel (discrete spectrum) provided by the GMR [59] and the other is a broadband channel (continuous spectrum) provided by the Fabry-Perot resonance in the HfO$_2$ slab. When $\delta = 1$, the reflection-type resonance peak is located at the wavelength $\lambda = 650$ nm, which slightly deviates from the predicted negative first-order resonance wavelength $\lambda_A = 640$ nm. This is because the grating above the waveguide layer will slightly change the effective refractive index of the waveguide layer [55]. As δ gradually decreases from unity to near zero, the resonance width of the peak reduces noticeably due to the decrease of the coupling between the negative first-order evanescent diffraction field and the leaky guided mode [60]. Meanwhile, the electric field intensity is enhanced within the waveguide layer due to the GMR mechanism and the field becomes more and more localized in the waveguide layer as the linewidth decreases. Note that the resonance peak slightly shifts toward long wavelengths because the refractive index distribution of the unit cell varies with δ. In the case of $\delta = 0$, the resonance width vanishes completely, which agrees with our prediction that a BIC appears as the guided mode becomes a dark mode. In addition, when δ is close to zero, the strongly localized resonance modes have ultranarrow resonance widths (i.e., ultrahigh Q factors) and these modes can be called quasi-BICs.

Furthermore, we calculate the resonance widths ($\Delta\lambda = |\lambda_{\text{peak}} - \lambda_{\text{dip}}|$) and obtain the corresponding Q factors ($Q = \lambda_{\text{peak}}/\Delta\lambda$) [37] for different values of δ, as shown
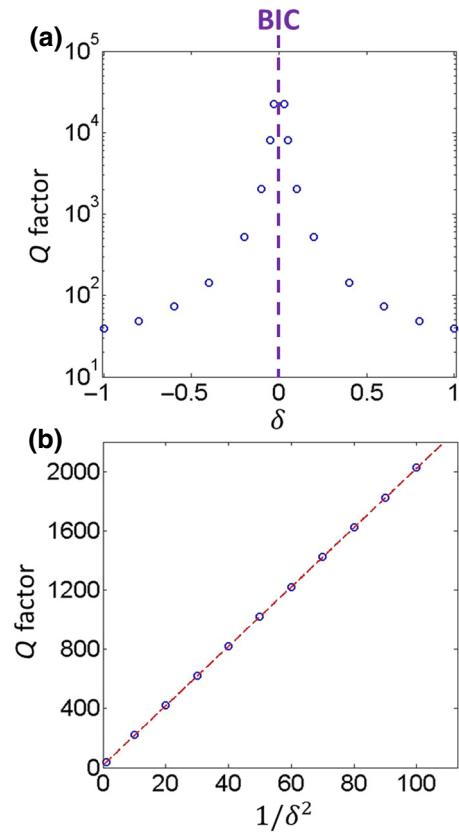

FIG. 4. (a) Dependence of Q factor on δ. (b) Linear relationship between Q factor and $1/\delta^2$. The red dashed line is a linear fitting line.

in Fig. 4(a). The Q factor for δ is identical to that for $-\delta$ due to the symmetry of the structure. When $\delta = \pm 1$, the Q factor is just 3.9×10^1. As δ gradually approaches to near zero, the Q factor increases rapidly. For example, the Q factor reaches 2.2×10^4 in the case of $\delta = \pm 0.03$. When δ is equal to zero, the resonance width vanishes completely and the Q factor becomes infinite. This case corresponds to BIC. If we use $1/\delta^2$ as the variable in the horizontal axis, in Fig. 4(b) we show that the Q factor is almost proportional to $1/\delta^2$, which is similar to Ref. [52].

In contrast, the reflectance spectra (zero-order diffraction) around the negative second-order resonance wavelength λ_B and the corresponding Q factors for different values of δ (see Appendix) show that the Q factors always keep finite values as the geometric parameter δ changes from 1 to 0. In other words, the BIC only appears around the negative first-order resonance wavelength λ_A but does not appear around the negative second-order resonance wavelength λ_B, which is accordance with our previous analysis based on the excitations of the guided resonance modes. In the following section, we will utilize the quasi-BIC (ultrahigh-Q-factor resonance) around λ_A to greatly enhance the GH shift.

III. GAINT GH SHIFT ASSISTED BY QUASI-BIC

In Fig. 3, we achieve quasi-BIC with ultranarrow resonance width in reflectance spectrum via tuning the geometric parameter δ to a near-zero value. Here, fixing the incident wavelength (denoted by λ_0) at the resonance peak in Fig. 3, we calculate the corresponding reflectance angular spectra when $\delta = 0.3$, 0.2, and 0.1, as shown in Figs. 5(a), 5(d), and 5(g), respectively. Comparing Fig. 3 with Figs. 5(a), 5(d), and 5(g), we can see that the narrower the resonance width in the reflectance spectrum is, the narrower the "resonance width" in the reflectance angular spectrum is. According to the stationary phase method, the GH shift for incident light with a sufficiently large beam waist (i.e., a narrow angular spectrum $\Delta k \ll k$) can be determined by [16,17,23]

$$S_{GH} = -\frac{\lambda_0}{2\pi}\frac{\partial \varphi_r}{\partial \theta}, \qquad (4)$$

where φ_r denotes the reflection phase. In other words, the GH shift is proportional to the partial derivative of the reflection phase to the incident angle. In Figs. 5(b), 5(e), and 5(h), we calculate the reflection phase angular spectra corresponding to Figs. 5(a), 5(d), and 5(g), respectively. From Eq. (4), the corresponding GH shift angular spectra are also given in Figs. 5(c), 5(f), and 5(i), respectively. It is seen that the reflection phase dramatically changes around the incident angle of the resonance peak ($\theta = 5°$), leading to a large GH shift at $\theta = 5°$. In addition, as the parameter δ decreases from 0.3 to 0.1, the peak value of the GH shift increases rapidly. The peak value of the GH shift reaches about $689\lambda_0$ when $\delta = 0.1$. Different from the large GH shift assisted by the Brewster dip [11–14] or transmission-type resonance [15–23], here, the maximum GH shift assisted by the quasi-BIC is located at the reflectance peak with unity reflectance, which can be more easily detected in the experiment.
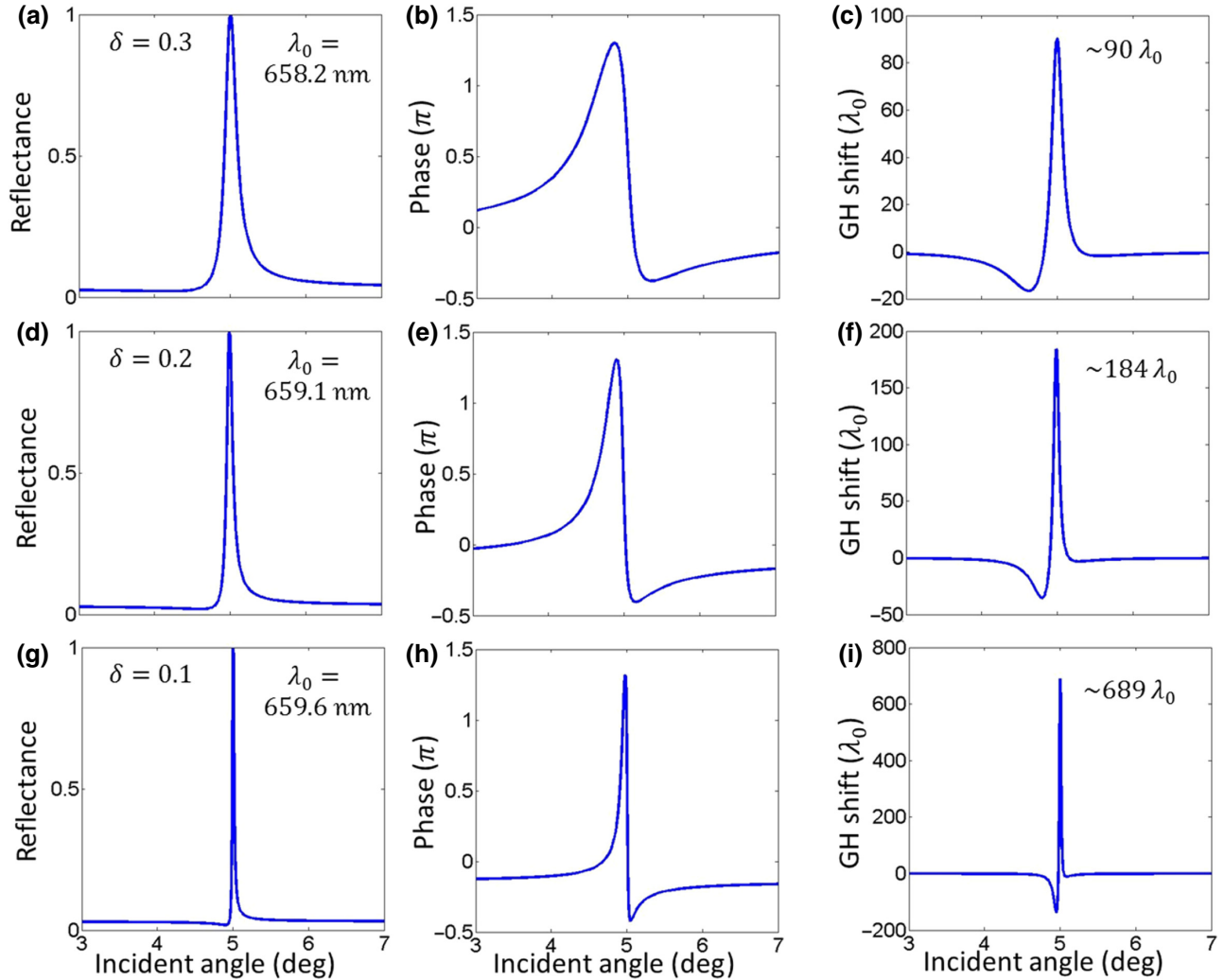

FIG. 5. Reflectance angular spectra for (a) $\delta = 0.3$ at $\lambda_0 = 658.2$ nm, (d) $\delta = 0.2$ at $\lambda_0 = 659.1$ nm, and (g) $\delta = 0.1$ at $\lambda_0 = 659.6$ nm. (b), (e), and (h): corresponding reflection phase angular spectra. (c), (f), and (i): corresponding GH shift angular spectra.
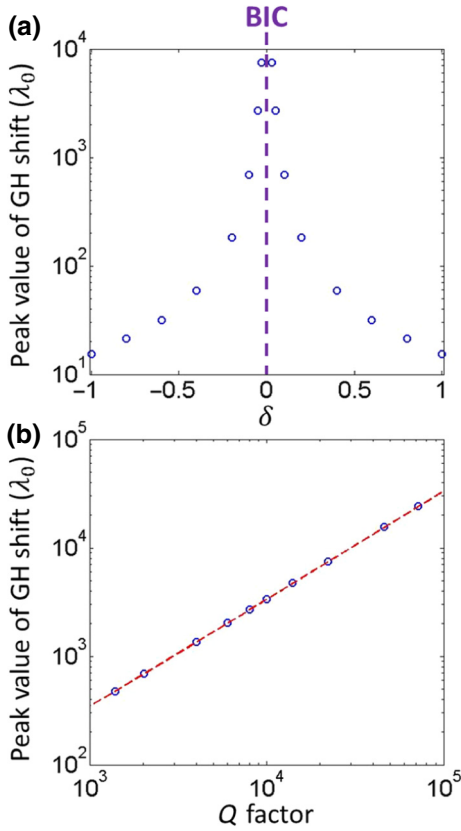
FIG. 6. (a) Dependence of peak value of GH shift on δ. (b) Linear relationship between peak value of GH shift and Q factor. The red dashed line is a linear fitting line.

In Fig. 6(a), we give the variation of the peak value of the GH shift as the geometric parameter δ changes from 1 to 0. Because of the symmetry of the structure, the peak value of the GH shift for δ is identical to that for $-\delta$. When $\delta = \pm 1$, the peak value of the GH shift is just about $1.5 \times 10^1 \lambda_0$. As δ gradually approaches to near zero, the peak value of the GH shift increases greatly. For example, the peak value of the GH shift reaches about $7.5 \times 10^3 \lambda_0$ in the case of $\delta = \pm 0.03$. It is seen that the dependence of the peak value of the GH shift on the parameter δ is very similar to that of the Q factor on δ [see Fig. 4(a)], indicating that the enhancement of the GH shift is closely related to the Q factor of the resonance.

Figure 6(b) gives the dependence of the peak value of the GH shift on the Q factor. The red dashed line is a linear fitting line. One can see that the peak value of the GH shift is nearly proportional to the Q factor. Because of the fabrication quality and finiteness of the structure, the experimentally measured Q factor will be lower than the theoretical one. Therefore, the experimental peak value of the GH shift will be also lower than the theoretical one. Under the current fabrication technique, the experimentally measured Q factor of the subwavelength grating

system based on the GMR mechanism can reach around the order of 10^4 [61,62]. Here, we choose the value of the Q factor to be 1.4×10^4 [62]. From Fig. 6(b), for this value of Q factor, the peak value of the GH shift can still reach $4.7 \times 10^3 \lambda_0$.

IV. ULTRASENSITIVE TEMPERATURE SENSOR

In this section, we design an ultrasensitive temperature sensor based on the quasi-BIC-assisted giant GH shift. As a kind of temperature-sensitive material, bismuth germanate ($Bi_4Ge_3O_{12}$) has a relatively high thermo-optical coefficient (in the order of $10^{-5}/°C$) at visible wavelengths [63]. Here, we choose it as the high-index medium in the four-part periodic grating layer as well as the waveguide layer. For the substrate, we still choose SiO_2. The schematic of the unit cell of the temperature sensor is given in Fig. 7(a). The incident plane is the x-O-z plane. We consider the TE-polarized light at oblique incidence. The operating wavelength is set to be $\lambda = 632.8$ nm.

The temperature-dependent refractive indices of $Bi_4Ge_3O_{12}$ and SiO_2 can be expressed in $n_1(T) = n_1(T_0) + \alpha_1(T - T_0)$ and $n_2(T) = n_2(T_0) + \alpha_2(T - T_0)$, where $T_0 = 25°C$ is room temperature, $n_1(T_0) = 2.097$ [64], and $n_2(T_0) = 1.457$ [65] represent the room-temperature refractive indices of $Bi_4Ge_3O_{12}$ and SiO_2, respectively, and $\alpha_1 = 3.9 \times 10^{-5}/°C$ [63] and $\alpha_2 = 9.6 \times 10^{-6}/°C$ [66] are the thermo-optical coefficients of $Bi_4Ge_3O_{12}$ and SiO_2, respectively. The geometric parameters at room temperature are designed to be $\Lambda(T_0) = 372$ nm (grating period), $d_a(T_0) = 0.2\Lambda(T_0)$, $d_b(T_0) = 0.285\Lambda(T_0)$, $d_c(T_0) = 0.315\Lambda(T_0)$, $h_1(T_0) = 228$ nm, and $h_2(T_0) = 150$ nm. Considering the thermal expansion effect, the temperature-dependent geometric parameters can be given by $\Lambda(T) = [1 + \beta_1(T - T_0)]\Lambda(T_0)$, $d_a(T) = 0.2\Lambda(T)$, $d_b(T) = 0.285\Lambda(T)$, $d_c(T) = 0.315\Lambda(T)$, $h_1(T) = [1 + \beta_1(T - T_0)]h_1(T_0)$, and $h_2(T) = [1 + \beta_1(T - T_0)]h_2(T_0)$, where $\beta_1 = 6.3 \times 10^{-6}/°C$ [63] represents the thermal expansion coefficient of $Bi_4Ge_3O_{12}$. Under the above design parameters, the corresponding Q factor $Q = 1.7 \times 10^4$ at room temperature can be extracted from the reflectance spectrum.

Based on the above parameters, the GH shift angular spectrum at room temperature $T_0 = 25°C$ is calculated, as shown by the black solid line in Fig. 7(b). At the incident angle of resonance peak ($\theta = 10°$), the GH shift reaches the maximum value of 1059 μm. For comparison, the GH shift angular spectrum at the temperature $T = 25.2°C$ (0.2°C deviation from room temperature) is also given by the blue dashed line in Fig. 7(b). It can be seen that the GH shift changes from 1059 μm to 748 μm ($\Delta \approx 311$ μm = 0.311 mm). At $\theta = 10°$, the temperature-dependent GH shift from 25°C to 26°C is shown in Fig. 7(c). As the
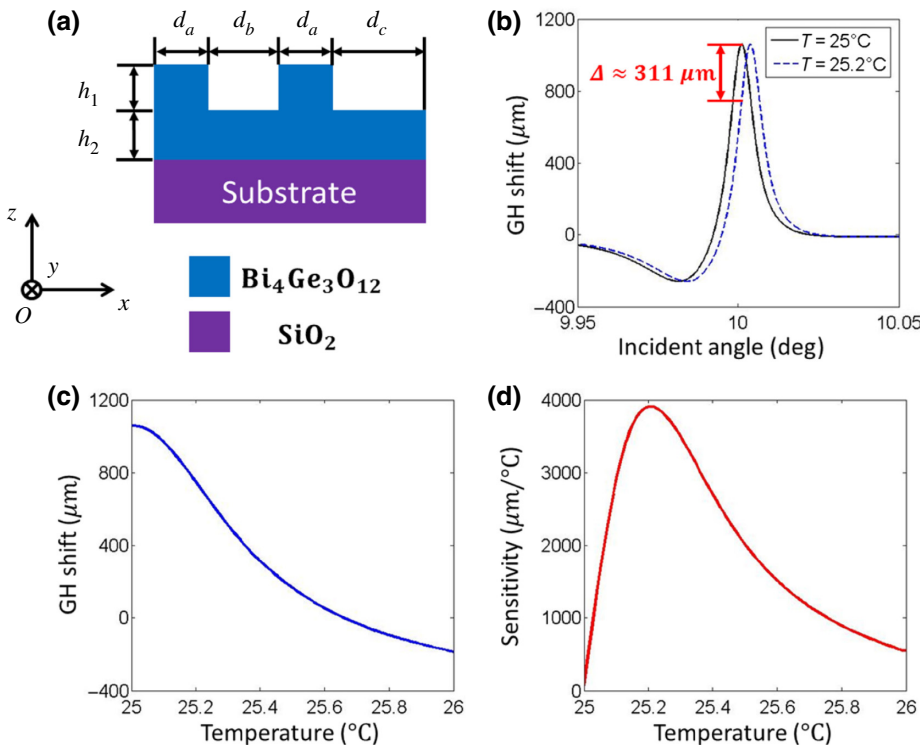
FIG. 7. (a) Schematic of the unit cell of the proposed temperature sensor. (b) GH shift angular spectra of the proposed sensor at $T = 25\,°C$ and $T = 25.2\,°C$. (c) GH shift of the proposed sensor versus temperature. (d) Temperature-dependent sensitivity of the proposed sensor.

temperature increases from 25°C to 26°C, the GH shift decreases from 1059 μm to -184 μm ($\Delta \approx 1243$ μm = 1.243 mm). In addition, the sensitivity of the proposed sensor (denoted by S) can be defined by the change rate (absolute value) of the GH shift with respect to the temperature, that is, $S(T) = |d(S_{GH})/dT|$. Figure 7(d) gives the dependence of the sensitivity on the temperature. The sensitivity is higher than 1×10^3 μm/°C when the temperature changes from 25.034°C to 25.760°C, indicating that the proposed temperature sensor can have ultrahigh sensitivity in a relatively wide temperature range. At the temperature $T = 25.212$°C, the sensitivity reaches the maximum value $S_{max} \approx 3907$ μm/°C. The temperature resolution of the proposed sensor depends on the position resolution of the GH shift that can be detected by the detector. Usually, the position resolution of the detector is about on the order of a micrometer [67]. Here, we suppose that the position resolution is 1.5 μm [67] and the temperature resolution is lower than 1×10^{-3} °C in the temperature range from 25.050 °C to 25.608 °C. The minimum temperature resolution of our proposed sensor reaches 3.8×10^{-4} °C at the temperature $T = 25.212$ °C, which is about one order higher than that in Ref. [2].

In order to show how the Q factor affects the performance of the proposed sensor, we change the geometric parameter $\delta = \Delta d/d$ to tune the Q factor and calculate the corresponding minimum temperature resolution, as shown in Fig. 8. Note that the operating angle is still chosen to be 10° and the operating wavelength is slightly deviated from $\lambda = 632.8$ nm. It can be seen that the minimum temperature resolution can reach 5.22×10^{-4} °C when the Q factor is supposed to be a practically achievable value of 1.4×10^4 [62].

So far, we have designed an ultrasensitive temperature sensor based on the enhanced GH shift by quasi-BICs. In addition to sensors, other applications based on the GH shift would also greatly benefit from the enhancement of the GH shift. For example, for a wavelength division demultiplexer based on the GH shift, the space separation
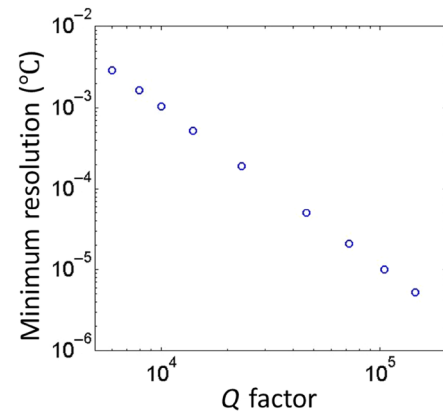

FIG. 8. Dependence of minimum temperature resolution on Q factor.

for the two reflected Gaussian beams with wavelengths of λ_1 and λ_2 is determined by $\Delta S_{GH} = |S_{GH,2} - S_{GH,1}|$ [6]. In this design, the larger the enhanced GH shift is, the better the performance of the wavelength division demultiplexing is.

V. CONCLUSIONS

In summary, we realize reflection-type BICs in the compound structure composed of a four-part periodic grating layer and a waveguide layer by tailoring the excitation of the guided modes. Assisted by the quasi-BIC, the GH shift can be greatly enhanced due to the ultrahigh-Q-factor resonance. The maximum GH shift is located at the reflectance peak with unity reflectance, which can be easily detected in the experiment. Based on the quasi-BIC-assisted giant GH shift, a variety of ultrasensitive sensors (e.g., temperature sensor, humidity sensor, and biosensor), light information storage devices, wavelength division de/multiplexers, optical switches, and polarization beam splitters can be designed.

APPENDIX

Here, we give the reflectance spectra (zero-order diffraction) around the negative second-order resonance wavelength $\lambda_B = 349$ nm, as shown in Fig. 9. When $\delta = 1$, the resonance peak is located at the wavelength $\lambda = 351$ nm, which slightly deviates from the predicted negative second-order resonance wavelength $\lambda_B = 349$ nm
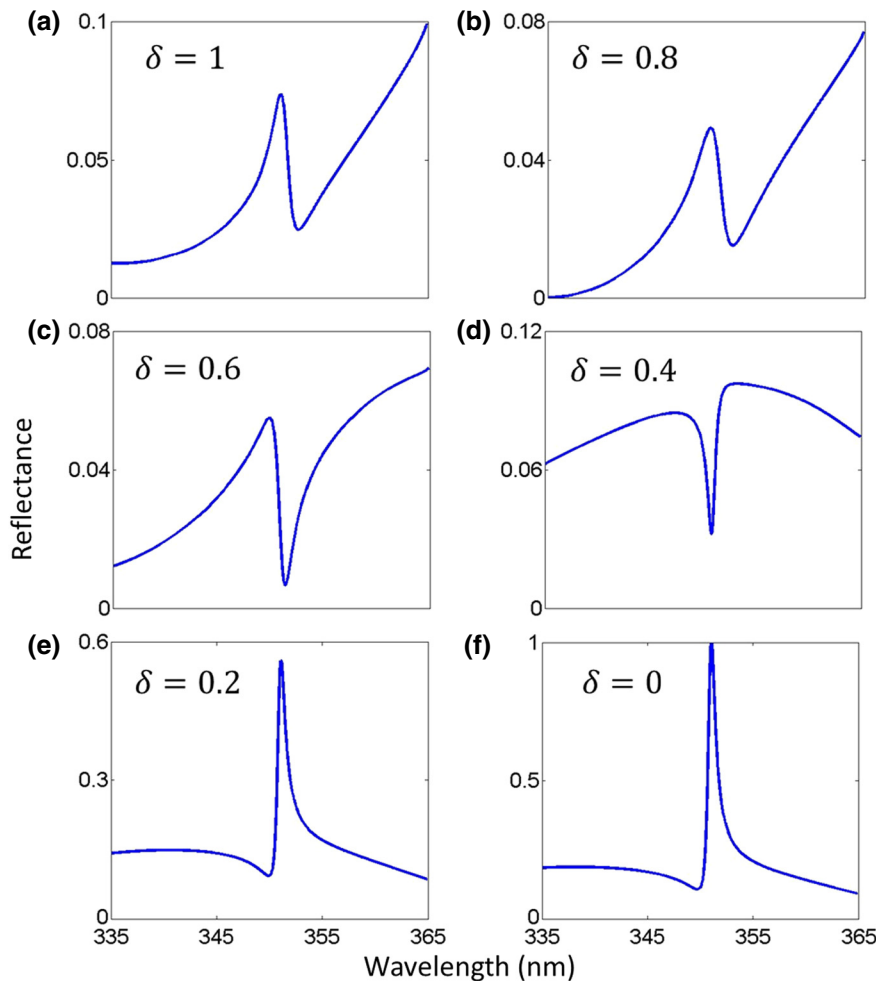

FIG. 9. Reflectance spectra around λ_B of the structure for different values of δ at $\theta = 5°$ for TE polarization.

because the grating above the waveguide layer will slightly change the effective refractive index of the waveguide layer [55].

One can see that the reflectance spectra exhibit strongly asymmetric Fano line types. Therefore, we use another method to extract the Q factor of the reflectance spectra. The reflectance spectrum of our system can be expressed as

$$R(\omega) = R_{\text{res}}(\omega) + R_{\text{bg}}(\omega). \qquad (A1)$$

The first term $R_{\text{res}}(\omega)$ represents the resonant contribution, which can be given by [68]

$$R_{\text{res}}(\omega) = F_0 \frac{[q + 2(\omega - \omega_0/\Gamma)]^2}{1 + [2(\omega - \omega_0/\Gamma)]^2}. \qquad (A2)$$

q, ω_0, and Γ are the asymmetric parameter, resonant angular frequency, and decay rate, respectively. The second term $R_{\text{bg}}(\omega)$ represents the background broadband contribution. In our system, it can be determined by the reflectance of the Fabry-Perot slab [69]

$$R_{\text{bg}}(\omega) = B_0 \frac{(\eta_0 - \eta_{\text{sub}})^2 \cos^2\phi_{\text{slab}} + [(\eta_0\eta_{\text{sub}}/\eta_{\text{slab}}) - \eta_{\text{slab}}]^2 \sin^2\phi_{\text{slab}}}{(\eta_0 + \eta_{\text{sub}})^2 \cos^2\phi_{\text{slab}} + [(\eta_0\eta_{\text{sub}}/\eta_{\text{slab}}) + \eta_{\text{slab}}]^2 \sin^2\phi_{\text{slab}}}. \qquad (A3)$$

$\eta_0 = \sqrt{n_0^2 - \sin^2\theta}$, $\eta_{\text{sub}} = \sqrt{n_{\text{sub}}^2 - \sin^2\theta}$ and $\eta_{\text{slab}} = \sqrt{n_{\text{slab}}^2 - \sin^2\theta}$ denote the impedances of air, substrate, and slab, respectively. $\phi_{\text{slab}} = (\omega/c)d_{\text{slab}}\sqrt{n_{\text{slab}}^2 - \sin^2\theta}$ denotes the propagating phase in the slab. In our system, $n_0 = 1$, $n_{\text{sub}} = 1.46$, and the incident angle is $\theta = 5°$.

Then we fit Eq. (A1) based on the reflectance data calculated by RCWA and finally obtain two of the fitting parameters, the resonant angular frequency ω_0 and the decay rate Γ. The corresponding Q factors for different values of δ can be determined by $Q = \omega_0/\Gamma$, as shown in Fig. 10. It can be seen that, different from the case of the negative first-order resonance wavelength, the Q factors always keep finite values (in the order of 10^2) as the geometric parameter δ changes from 1 to 0. Therefore, there is no BIC around the negative second-order resonance wavelength λ_B.
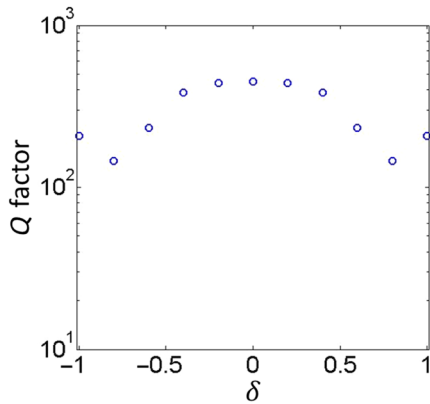

FIG. 10. Dependence of Q factor on δ.

[1] F. Goos and H. Hänchen, Ein neuer und fundamentaler Versuch zur Totalreflexion, Ann. Phys. **436**, 333 (1947).

[2] X. Wang, C. Yin, J. Sun, H. Li, Y. Wang, M. Ran, and Z. Cao, High-sensitivity temperature sensor using the ultrahigh order mode-enhanced Goos-Hänchen effect, Opt. Express **21**, 13380 (2013).

[3] T. Yu, H. Li, Z. Cao, Y. Wang, Q. Shen, and Y. He, Oscillating wave displacement sensor using the enhanced Goos-Hänchen effect in a symmetrical metal-cladding optical waveguide, Opt. Lett. **33**, 1001 (2008).

[4] X. Wang, M. Sang, W. Yuan, Y. Nie, and H. Luo, Optical Relative Humidity Sensing Based on Oscillating Wave-Enhanced Goos-Hänchen Shift, IEEE Photonics Technol. Lett. **28**, 264 (2016).

[5] K. L. Tsakmakidis, A. D. Boardman, and O. Hess, 'Trapped rainbow' storage of light in metamaterials, Nature **450**, 397 (2007).

[6] H. Sattari, S. E. Bakhtevar, and M. Sahrai, Proposal for a 1×3 Goos-Hänchen shift-assisted de/multiplexer based on a multilayer structure containing quantum dots, J. Appl. Phys. **120**, 133102 (2016).

[7] T. Sakata, H. Togo, and F. Shimokawa, Reflection-type 2×2 optical waveguide switch using the Goos-Hänchen shift effect, Appl. Phys. Lett. **76**, 2841 (2000).

[8] X. Wang, C. Yin, J. Sun, J. Gao, M. Huang, and Z. Cao, Reflection-type space-division optical switch based on the electrically tuned Goos–Hänchen effect, J. Opt. **15**, 2040 (2013).

[9] X. Chen, M. Shen, Z. Zhang, and C. Li, Tunable lateral shift and polarization beam splitting of the transmitted light beam through electro-optic crystals, J. Appl. Phys. **104**, 123101 (2008).

[10] K. Artmann, Berechnung der Seitenversetzung des totalreflektierten Strahles, Ann. Phys. **437**, 87 (1948).

[11] H. M. Lai and S. W. Chan, Large and negative Goos-Hänchen shift near the Brewster dip on reflection from weakly absorbing media, Opt. Lett. **27**, 680 (2002).

[12] L. Jiang, Q. Wang, Y. Xiang, X. Dai, and S. Wen, Electrically Tunable Goos-Hänchen Shift of Light Beam Reflected From a Graphene-on-Dielectric Surface, IEEE Photonics J. **5**, 6500108 (2013).

[13] C. Xu, J. Xu, G. Song, C. Zhu, Y. Yang, and G. S. Agarwal, Enhanced displacements in reflected beams at hyperbolic metamaterials, Opt. Express **24**, 21767 (2016).

[14] Y. Y. Huang, W. T. Dong, L. Gao, and C. W. Qiu, Large positive and negative lateral shifts near pseudo-Brewster dip on reflection from a chiral metamaterial slab, Opt. Express **19**, 1310 (2011).

[15] R. Kaiser, Y. Levy, J. Fleming, S. Muniz, and V. S. Bagnato, Resonances in a single thin dielectric layer: enhancement of the Goos-Hänchen shift, Pure Appl. Opt. **5**, 891 (1996).

[16] L. Wang, H. Chen, and S. Zhu, Large negative Goos-Hänchen shift from a weakly absorbing dielectric slab, Opt. Lett. **30**, 2936 (2005).

[17] L. Wang and S. Zhu, Giant lateral shift of a light beam at the defect mode in one-dimensional photonic crystals, Opt. Lett. **31**, 101 (2006).

[18] X. Yin, L. Hesselink, Z. Liu, N. Fang, and X. Zhang, Large positive and negative lateral optical beam displacements due to surface plasmon resonance, Appl. Phys. Lett. **85**, 372 (2004).

[19] V. J. Yallapragada, A. P. Ravishankar, G. L. Mulay, G. S. Agarwal, and V. G. Achanta, Observation of giant Goos-Hänchen and angular shifts at designed metasurfaces, Sci. Rep. **6**, 19319 (2016).

[20] C. Li and Q. Wang, Prediction of simultaneously large and opposite generalized Goos-Hänchen shifts for TE and TM light beams in an asymmetric double-prism configuration, Phys. Rev. E **69**, 055601(R) (2004).

[21] Y. Wong, Y. Miao, J. Skarda, and O. Solgaard, Large negative and positive optical Goos-Hänchen shift in photonic crystals, Opt. Lett. **43**, 2803 (2018).

[22] Y. Wan, Z. Zheng, W. Kong, X. Zhao, Y. Liu, Y. Bian, and J. Liu, Nearly three orders of magnitude enhancement of Goos-Hänchen shift by exciting Bloch surface wave, Opt. Express **20**, 8998 (2012).

[23] J. Wen, J. Zhang, L. Wang, and S. Zhu, Goos-Hänchen shifts in an epsilon-near-zero slab, J. Opt. Soc. Am. B **34**, 2310 (2017).

[24] K. N. Pichugin, D. N. Maksimov, and A. F. Sadreev, Goos-Hänchen and Imbert-Fedorov shifts of higher-order Laguerre-Gaussian beams reflected from a dielectric slab, J. Opt. Soc. Am. A **35**, 1324 (2018).

[25] H. Y. Li, F. Honary, Z. S. Wu, and L. Bai, Reflection and transmission of Laguerre-Gaussian beams in a dielectric slab, J. Quant. Spectrosc. Radiat. Transfer **195**, 35 (2017).

[26] C. W. Hsu, B. Zhen, A. D. Stone, J. D. Joannopoulos, and M. Soljačić, Bound state in the continuum, Nat. Rev. Mater. **1**, 16048 (2016).

[27] H. Friedrich and D. Wintgen, Physical realization of bound states in the continuum, Phys. Rev. A **31**, 3964 (1985).

[28] H. Friedrich and D. Wintgen, Interfering resonances and bound states in the continuum, Phys. Rev. A **32**, 3231 (1985).

[29] E. N. Bulgakov and A. F. Sadreev, Bound states in the continuum in photonic waveguides inspired by defects, Phys. Rev. B **78**, 075105 (2008).

[30] Y. Plotnik, O. Peleg, F. Dreisow, M. Heinrich, S. Nolte, A. Szameit, and M. Segev, Experimental Observation of Optical Bound States in the Continuum, Phys. Rev. Lett. **107**, 183901 (2011).

[31] D. C. Marinica and A. G. Borisov, Bound States in the Continuum in Photonics, Phys. Rev. Lett. **100**, 183902 (2008).

[32] A. Kodigala, T. Lepetit, Q. Gu, B. Bahari, Y. Fainman, and B. Kanté, Lasing action from photonic bound states in continuum, Nature **541**, 196 (2017).

[33] K. Hirose, Y. Liang, Y. Kurosaka, A. Watanabe, T. Sugiyama, and S. Noda, Watt-class high-power, high-beam-quality photonic-crystal lasers, Nat. Photonics **8**, 406 (2014).

[34] J. M. Foley, S. M. Young, and J. D. Phillips, Symmetry-protected mode coupling near normal incidence for narrow-band transmission filtering in a dielectric grating, Phys. Rev. B **89**, 165111 (2014).

[35] M. Zhang and X. Zhang, Ultrasensitive optical absorption in graphene based on bound states in the continuum, Sci. Rep. **5**, 8266 (2015).

[36] M. I. Molina, A. E. Miroshnichenko, and Y. S. Kivshar, Surface Bound States in the Continuum, Phys. Rev. Lett. **108**, 070401 (2012).

[37] Y. Zhang, W. Liu, Z. Li, Z. Li, H. Cheng, S. Chen, and J. Tian, High-quality-factor multiple Fano resonances for refractive index sensing, Opt. Lett. **43**, 1842 (2018).

[38] S. Romano, G. Zito, S. Torino, G. Calafiore, E. Penzo, G. Coppola, S. Cabrini, I. Rendina, and V. Mocella, Label-free sensing of ultralow-weight molecules with all-dielectric metasurfaces supporting bound states in the continuum, Photonics Res. **6**, 726 (2018).

[39] Y. Wang, Md. A. Ali, E. K. C. Chow, L. Dong, and M. Lu, An optofluidic metasurface for lateral flow-through detection of breast cancer biomarker, Biosens. Bioelectron. **107**, 224 (2018).

[40] H. M. Doeleman, F. Monticone, W. den Hollander, A. Alù, and A. F. Koenderink, Experimental observation of a polarization vortex at an optical bound state in the continuum, Nat. Photonics **12**, 397 (2018).

[41] F. Monticone and A. Alù, Bound states within the radiation continuum in diffraction gratings and the role of leaky modes, New J. Phys. **19**, 093011 (2017).

[42] L. Ni, Z. Wang, C. Peng, and Z. Li, Tunable optical bound states in the continuum beyond in-plane symmetry protection, Phys. Rev. B **94**, 245148 (2016).

[43] J. W. Yoon, S. H. Song, and R. Magnusson, Critical field enhancement of asymptotic optical bound states in the continuum, Sci. Rep. **5**, 18301 (2015).

[44] E. N. Bulgakov, D. N. Maksimov, P. N. Semina, and S. A. Skorobogatov, Propagating bound states in the continuum in dielectric gratings, J. Opt. Soc. Am. B **35**, 1218 (2018).

[45] Y. Wang, J. Song, L. Dong, and M. Lu, Optical bound states in slotted high-contrast gratings, J. Opt. Soc. Am. B **33**, 2472 (2016).

[46] Z. F. Sadrieva, I. S. Sinev, K. L. Koshelev, A. Samusev, I. V. Iorsh, O. Takayama, R. Malureanu, A. A. Bogdanov, and A. V. Lavrinenko, Transition from Optical Bound States in the Continuum to Leaky Resonances: Role of Substrate and Roughness, ACS Photonics **4**, 723 (2017).

[47] C. W. Hsu, B. Zhen, J. Lee, S. Chua, S. G. Johnson, J. D. Joannopoulos, and M. Soljačić, Observation of trapped light within the radiation continuum, Nature **499,** 188 (2013).

[48] M. Minkov, I. A. D. Williamson, M. Xiao, and S. Fan, Zero-Index Bound States in the Continuum, Phys. Rev. Lett. **121,** 263901 (2018).

[49] E. Penzo, S. Romano, Y. Wang, S. Dhuey, L. D. Negro, V. Mocella, and S. Cabrini, Patterning of electrically tunable light-emitting photonic structures demonstrating bound states in the continuum, J. Vac. Sci. Technol. B **35,** 0401 (2017).

[50] S. Romano, G. Zito, S. Managò, G. Calafiore, E. Penzo, S. Cabrini, A. C. De Luca, and V. Mocella, Surface-Enhanced Raman and Fluorescence Spectroscopy with an All-Dielectric Metasurface, J. Phys. Chem. C **122,** 19738 (2018).

[51] B. Zhen, S. Chua, J. Lee, A. W. Rodriguez, X. Liang, S. G. Johnson, J. D. Joannopoulos, M. Soljačić, and O. Shapira, Enabling enhanced emission and low-threshold lasing of organic molecules using special Fano resonances of macroscopic photonic crystals, Proc. Natl. Acad. Sci. USA **110,** 13711 (2013).

[52] K. Koshelev, S. Lepeshov, M. Liu, A. Bogdanov, and Y. Kivshar, Asymmetric Metasurfaces with High-Q Resonances Governed by Bound States in the Continuum, Phys. Rev. Lett. **121,** 193903 (2018).

[53] P. S. Priambodo, T. A. Maldonado, and R. Magnusson, Fabrication and characterization of high-quality waveguide-mode resonant optical filters, Appl. Phys. Lett. **83,** 3248 (2003).

[54] Y. Wang, X. Gao, Z. Shi, L. Chen, M. L. Garcia, N. A. Hueting, M. Cryan, X. Li, M. Zhang, and H. Zhu, Guided-Mode Resonant HfO_2 Grating at Visible Wavelength Range, IEEE Photonics J. **6,** 2200407 (2014).

[55] T. Sang, S. Cai, and Z. Wang, Guided-mode resonance filter with an antireflective surface consisting of a buffer layer with refractive index equal to that of the grating, J. Mod. Opt. **58,** 1260 (2011).

[56] A. Yariv and P. Yeh, *Optical waves in crystals* (Wiley, New York, 1984).

[57] M. G. Moharam, D. A. Pommet, E. B. Grann, and T. K. Gaylord, Stable implementation of the rigorous coupled-wave analysis for surface-relief gratings: enhanced

transmittance matrix approach, J. Opt. Soc. Am. A **12,** 1077 (1995).

[58] A. E. Miroshnichenko, S. Flach, and Y. S. Kivshar, Fano resonances in nanoscale structures, Rev. Mod. Phys. **82,** 2257 (2010).

[59] G. Zheng, X. Zou, Y. Chen, L. Xu, and Y. Liu, Tunable Spectrum Selective Enhanced Absorption of Monolayer Graphene in Fano Resonant Waveguide Grating with four-Part Period, Plasmonics **12,** 1177 (2017).

[60] W. Liu, Y. Li, H. Jiang, Z. Lai, and H. Chen, Controlling the spectral width in compound waveguide grating structures, Opt. Lett. **38,** 163 (2013).

[61] Y. Shuai, D. Zhao, Z. Tian, J. Seo, D. V. Plant, Z. Ma, S. Fan, and W. Zhou, Double-layer Fano resonance photonic crystal filters, Opt. Express **21,** 2458 (2013).

[62] Y. Zhou, M. Moewe, J. Kern, M. C. Y. Huang, and C. J. Chang-Hasnain, Surface-normal emission of a high-Q resonator using a subwavelength high-contrast grating, Opt. Express **16,** 17282 (2008).

[63] P. A. Williams, A. H. Rose, K. S. Lee, D. C. Conrad, G. W. Day, and P. D. Hale, Optical, thermo-optic, electro-optic, and photoelastic properties of bismuth germanate ($Bi_4Ge_3O_{12}$), Appl. Opt. **35,** 3562 (1996).

[64] G. Montemezzani, St. Pfändler, and P. Günter, Electro-optic and photorefractive properties of $Bi_4Ge_3O_{12}$ crystals in the ultraviolet spectral range, J. Opt. Soc. Am. B **9,** 1110 (1992).

[65] E. Palik, *Handbook of Optical Constants of Solids* (Academic, New York, 1998).

[66] A. W. Elshaari, I. E. Zadeh, K. D. Jöns, and V. Zwiller, Thermo-Optic Characterization of Silicon Nitride Resonators for Cryogenic Photonic Circuits, IEEE Photonics J. **8,** 2701009 (2016).

[67] Y. Wang, H. Li, Z. Cao, T. Yu, Q. Shen, and Y. He, Oscillating wave sensor based on the Goos-Hänchen effect, Appl. Phys. Lett. **92,** 061117 (2008).

[68] M. Galli, S. L. Portalupi, M. Belotti, L. C. Andreani, L. O'Faolain, and T. F. Krauss, Light scattering and Fano resonances in high-Q photonic crystal nanocavities, Appl. Phys. Lett. **94,** 071101 (2009).

[69] P. Yeh, *Optical Waves in Layered Media* (Wiley, New York, 1988).